Nano Energy 79 (2021) 105459

Contents lists available at ScienceDirect

Nano Energy

journal homepage: http://www.elsevier.com/locate/nanoen

Full paper

In-situ surface chemical and structural self-reconstruction strategy enables high performance of Li-rich cathode

Gang Sun [a,b,d], Changtai Zhao [d], Fu-Da Yu [b], Ruizhi Yu [d], Jian Wang [c], Jigang Zhou [c], Guangjie Shao [a,*], Xueliang Sun [d,*], Zhen-Bo Wang [b,*]

[a] State Key Laboratory of Metastable Materials Science and Technology, Hebei Key Laboratory of Heavy Metal Deep-Remediation in Water and Resource Reuse, College of Environmental and Chemical Engineering, Yanshan University, Qinhuangdao 066004, China
[b] MIIT Key Laboratory of Critical Materials Technology for New Energy Conversion and Storage, State Key Lab of Urban Water Resource and Environment, School of Chemistry and Chemical Engineering, Harbin Institute of Technology, No. 92 West-Da Zhi Street, Harbin 150001, China
[c] Canadian Light Source Inc., University of Saskatchewan, Saskatoon, SK S7N 2V3, Canada
[d] Department of Mechanical and Materials Engineering, University of Western Ontario, London, Ontario N6A 5B9, Canada

ARTICLE INFO

Keywords:
Li-rich cathodes
Surface treatment
Surface self-reconstruction
Multifunction protective layer
High energy density Li-ion batteries

ABSTRACT

The critical challenges hindering the commercialization of Li-rich cathodes are their rapid-decaying capacity and voltage during cycling, originating from the degradation of lattice structure and interface side reaction between electrode and electrolyte. Surface engineering is considered to be an effective strategy to mitigate these disadvantages. Herein, an *in-situ* self-reconstruction strategy is proposed and developed to simultaneously optimize surface chemical composition and local structure of Li-rich cathodes. Specifically, the multifunction protective layer consisting of cation disorder phase and $LiTMPO_4$-like (TM: Ni, Co, Mn) phase is produced by a simple PH_3 gas treatment. $LiTMPO_4$ featuring the ability against high potential is responsible for preventing interface side reaction and further reduce the dissolution of Mn. Both $LiTMPO_4$-like phase and surface cation disorder phase contribute to stabilizing surface oxygen structure and limiting surface O_2 release. Compared to the pristine one, better integrity of chemical phases and higher oxidation state of TM cations after long-term cycling are confirmed in the modified sample by synchrotron-based scanning transmission X-ray microscopy, highlighting the key roles of the multifunction protective layer in stabilizing the capacity and voltage during cycling. This surface self-reconstruction strategy provides a new path for guiding the interface design of high energy density cathodes.

1. Introduction

The development of rechargeable batteries has greatly eased the pressures on energy shortages and environmental pollution caused by the burning of fossil fuels [1–3]. Lithium-ion batteries (LIBs) with high gravimetric and volumetric energy density are recognized as the most promising candidate for next-generation rechargeable batteries. The poor performance of cathode materials in terms of low available capacities and cycling stability has been considered to be the major bottlenecks for upgrading the energy density of LIBs [4–8]. Therefore, cathodes with low cost, high specific capacity, high discharge voltage, excellent cycling stability, and environmental friendliness become the pursuit of developing future LIBs. Among the cathode families of LIBs, Mn-based Li-rich cathode materials ($aLi_2MnO_3{\cdot}(1-a)LiMn_xNi_yCo_zO_2$, $x + y + z = 1$, LR-NCMs) have attracted intensive research interests due to their high reversible capacities (~ 250 mA h g^{-1}) and low cost [9–11]. The extraordinary capacity of LR-NCMs is attributed to multiple electrons redox reaction processes containing cationic and anionic (lattice oxygen participates in charge compensation) redox processes [12]. The lattice oxygen activity takes place at a high potential (~ 4.5 V) in the form of reversible bulk oxygen redox ($O^{2-} \rightarrow O^{n-}$, $n < 2$), bringing about higher capacity [13,14]. However, it is always accompanied by irreversible O_2 release mainly occurring at the electrode surface, which triggers the degradation of surface lattice structure and reduction of transition metal (TM) cations and further results in voltage fade and capacity decay [15–17]. Recently, combining physical characterizations including hard-X-ray photoelectron spectroscopy (XPS) or scanning transmission X-ray microscopy (STXM) with electrochemical analysis (voltage window experiments), studies [16,18–20] confirmed the redox reactivity of lattice oxygen in LR-NCMs and further correlated it with the

* Corresponding authors.
E-mail addresses: shaoguangjie@ysu.edu.cn (G. Shao), xsun9@uwo.ca (X. Sun), wangzhb@hit.edu.cn (Z.-B. Wang).

https://doi.org/10.1016/j.nanoen.2020.105459
Received 31 August 2020; Received in revised form 27 September 2020; Accepted 3 October 2020
Available online 8 October 2020

sluggish kinetics. It is worth noting that the cation migration may result from the unstable structure after oxygen oxidation at high potential, related to its voltage decay. Moreover, the irreversible oxygen loss (O_2 release) from the surface to the bulk of LR-NCMs causes the reduction of the average valence state of TM cations (activating the low-potential $Mn^{3+/4+}$ and $Co^{2+/3+}$ redox couples) and microstructural defects (the formation of large pores within particles), which directly lead to the voltage and capacity decay [15]. Furthermore, at a high potential, the highly active oxygen at the interface of the LR-NCMs triggers serious interface problems such as the undesired electrode-electrolyte side reactions, electrolyte decomposition, surface corrosion and dissolution of the cathode [21]. To further promote the development of LR-NCMs, the next work needs to focus on the stabilization of the lattice oxygen to reduce the oxygen loss, and the improvement of interface stability between the electrode and electrolyte to reduce the undesired side reactions.

A series of effective strategies have been proposed to address the above-mentioned problems [22–25]. For instance, the lattice oxygen chemistry and the release of O_2 at the surface of LR-NCMs can be manipulated through optimizing the microstructure (adjusting the ratio of Li_2MnO_3 and $LiTMO_2$ phase component of LR-NCMs) [26] and chemical composition of LR-NCMs (introducing Ni^{2+} as a redox buffer) [27–30], enhancing the operating voltage as well as suppressing the capacity and voltage decay. However, the issues of the interface instability at high potential remained in these approaches. Surface modification, including surface coating [31–34], water or weak acid treatment [35], oxygen vacancy, and heterogeneous surface structure [36–38], have been proved as an effective strategy to ameliorate aforementioned issues. Recently, researchers reported a simple gas-solid interface reaction, which simply exposed LR-NCMs in CO_2 [39], NH_3 [40], or sulfur [41] atmosphere at low temperature (100–400 °C) to increase the oxygen vacancies, form the oxygen-deficient spinel-like phase at the surface of LR-NCMs. This could enhance the capacity and mitigate the voltage decay. Anyway, a stable surface/interface at high potential is indispensable for LR-NCMs to suppress the interface side reaction and reducing the oxygen release. According to previous reports [42–44], the rather strong P–O bonds in polyanion $(PO_4)^{3-}$ is covalently bonded to chemically stabilize $TM^{2+/3+}$. This ensures the compounds ($LiTMPO_4$) electrochemically stable at high electrical potential and a higher cationic redox reaction potential, like 4.8 V for $LiCoPO_4$, 4.1 V for $LiMnPO_4$ and 5.1 V for $LiNiPO_4$, etc. [45]. $LiTMPO_4$ serves as a potential surface coating layer of LR-NCMs but it is difficult to form a uniform coating. Therefore, a simple yet effective strategy to prepare a protective layer with the ability against high potential on the surface of LR-NCMs is highly required. A promising strategy arises, that is, an *in-situ* introduction of a phosphorus-containing protective layer on the surface of LR-NCMs, which could effectively improve the interface stability and inhibit the O_2 release at the surface under high potential.

Following the above considerations, we are proposing a simple yet effective method involving a PH_3 gas-solid treatment of LR-NCMs at low temperature (300 °C) to form an *in-situ* phosphorus-containing compound protective layer, which ensures the integrity of both protective layer and bulk structure. The process of surface modification is shown in Scheme 1a. In this work, we used low-Co and high-Ni content Li-rich cathode ($Li_{1.17}Mn_{0.44}Ni_{0.34}Co_{0.04}O_2$, LNCM) to conduct surface engineering due to the higher operating voltage [30]. The unique $LiTMPO_4$-like phase and the cation disorder phase were formed by an *in-situ* surface chemical and structural self-reconstruction of LR-NCMs particles (as shown in Scheme 1d). As a result, the PH_3-treated LNCM (P-LNCM) shows higher capacity retention and lower voltage degradation than those of pristine LNCM, together delivering a significantly improved energy density retention. Moreover, the electrochemical analysis and various physical characterization techniques including spatially resolved synchrotron-based STXM with soft X-ray absorption spectrum (sXAS) were combined to comprehensively investigate the effect and mechanism of this protective layer for enhancing the stability of cathode materials.

2. Experimental section

2.1. Material synthesis

The Low-Co and High-Ni content Li-Rich cathode material $Li_{1.17}Mn_{0.44}Ni_{0.35}Co_{0.04}O_2$ was first prepared by carbonate co-precipitation and followed by a solid-state method [30,33]. Carbonate precursor $Mn_{0.44}Ni_{0.35}Co_{0.04}(CO_3)_{0.8}$ was obtained by co-precipitation reaction. Stoichiometric $NiSO_4{\cdot}6H_2O$, $CoSO_4{\cdot}7H_2O$, and $MnSO_4{\cdot}6H_2O$ were dissolved in deionized water forming a 2 M TM sulfate aqueous solution A. The mixed Na_2CO_3 (2 M) and $NH_3{\cdot}H_2O$ (0.2 M) aqueous solution were marked as solution B. The two solutions were then added

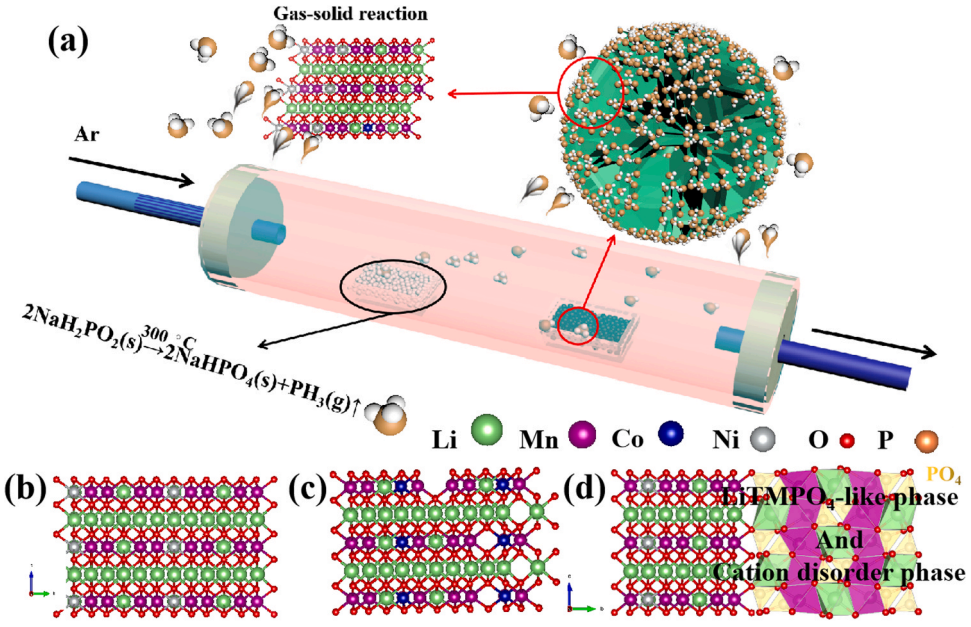

Scheme 1. (a) Schematic diagram of the surface modification process; Crystal structure of (b) LNCM without any modification; (c) LNCM treated at 300 °C in Ar atmosphere, (d) LNCM with surface modification.

dropwise to the continuous reactor C, respectively. The mixed solution in the continuous reactor C was conducted under the controlled conditions and maintained for 15 h to confirm the morphology and homogeneity of secondary particles. The obtained carbonate precursors were ground with an appropriate amount of Li_2CO_3, and then sintering was carried out at 500 °C for 5 h and 850 °C for 12 h, and finally, the obtained powder was named LNCM sample with the structural diagram shown in Scheme 1b.

2.2. PH_3 treatment sample

the PH_3 gas was obtained by a pyrolysis reaction of sodium hypophosphite (NaH_2PO_2), as shown in the following equation, $\mathbf{2NaH_2PO_2(s) \rightarrow Na_2HPO_4(s) + PH_3(g)\uparrow}$ (*s* represents for solid, and *g* represents for gas). The LNCM sample and sodium hypophosphite were separately packed in two crucibles with a certain mass ratio and then heated at 300 °C, 2 h under Ar atmosphere, as shown in Scheme 1a. The obtained modified material was named as P-LNCM and the structural diagram is shown in Scheme 1e. Meanwhile, part of the LNCM powder was heated without PH_3(g) at 300 °C, 2 h under Ar atmosphere, as a comparative sample named Ar-300 sample (Scheme 1c).

The material characterizations and electrochemical measurements section are shown in the Supporting information.

3. Results and discussion

The microstructure and elemental composition of the as-prepared samples were investigated by the Focused ion beam/Scanning electron microscopy (FIB/SEM) and inductively coupled plasma-optical emission spectroscopy (ICP-OES), and the results are shown in Fig. S1 and Table S1 in the Supporting information. From the results of elemental analysis, it can be found that the proportion of Li in P-LNCM was slightly decreased due to the loss of Li_2O during the surface treatment process, and a small amount of P element is present in the P-LNCM sample, indicating that P was successfully introduced into the modified material. The distribution of P element in P-LNCM particle was probed by the Energy Dispersive Spectrometer (EDS) line scan on the cross-section of a P-LNCM particle made by FIB, displayed in Fig. 1a and b. The results show that the P element is mainly distributed on the surface of the P-LNCM particle, and the abundance decreased with increasing depth. This is also in agreement with the ICP-OES result that just a small amount of P element exists in P-LNCM. The P chemical state and structure information of P-LNCM was investigated by XPS, X-ray diffraction (XRD), Raman, and Fourier transform infrared spectrum (FTIR). Fig. 1c shows the XPS survey spectra. It is noted that there are Ni, Co, Mn, O, and Li in both pristine LNCM and P-LNCM samples, but the P signal can only be found in the spectrum of P-LNCM, which also confirms the existence of P in the modified material. The main peak of the P 2p spectrum centered at 135.25 eV corresponds to the P-O bond in $(PO_4)^{3-}$ groups (Fig. 1d) [46,47]. This indicates the presence of $(PO_4)^{3-}$ groups at the surface of particles after surface modification. This can also be confirmed by FTIR result (Fig. 1e), where the small vibrations around 950 and 1180 cm^{-1} are assigned to the asymmetric stretching P–O vibrations and P–O–P bridging vibration in $(PO_4)^{3-}$ group, respectively [48,49]. From the core-level spectra of Ni 2p shown in Fig. 1f, Ni $2p_{3/2}$ peaks with a binding energy of 854.9 and 856.2 eV are in good

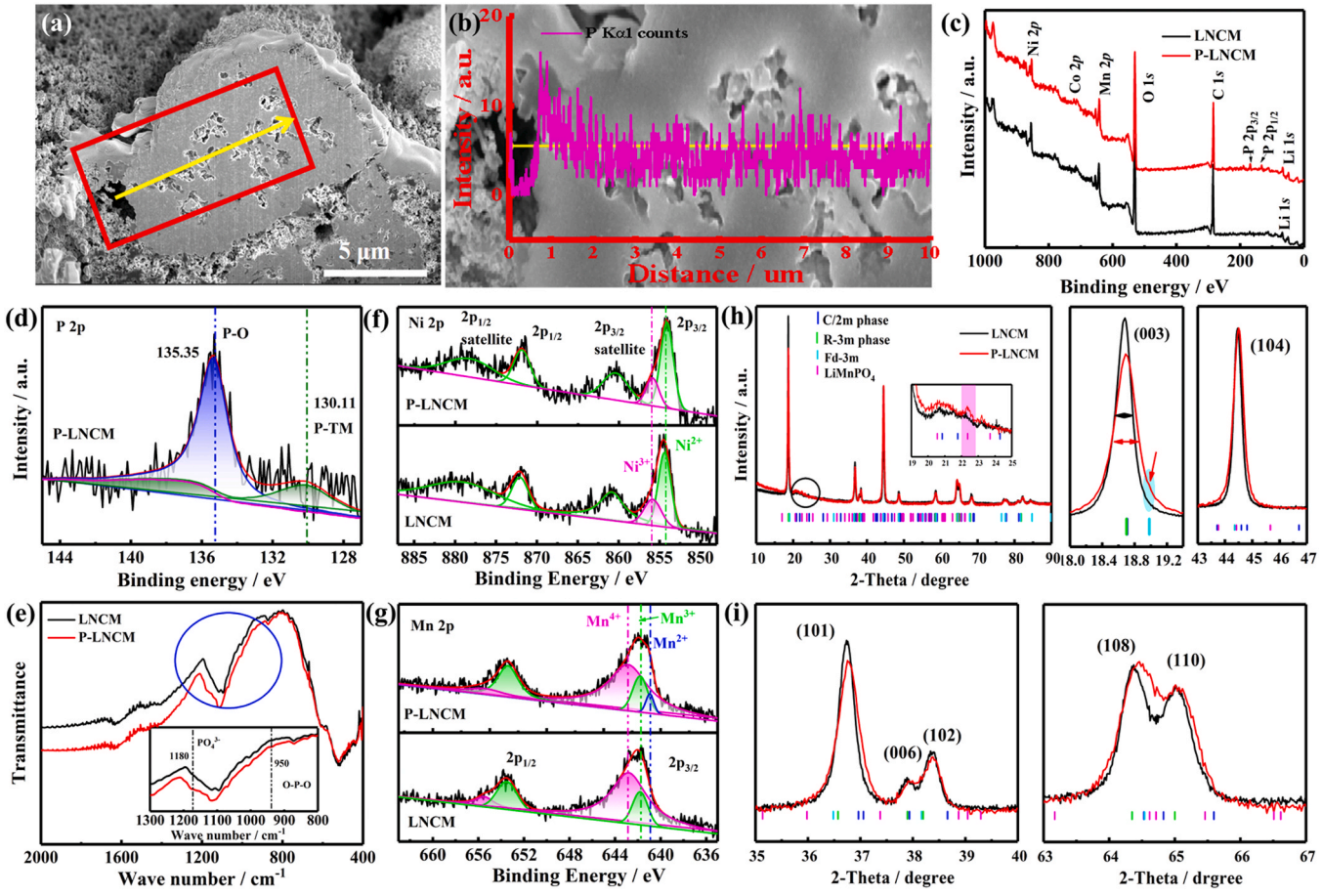

Fig. 1. The cross-section FIB/SEM image (a) with the EDS line scan with the P Kα1 signal (b) of a P-LNCM particle. (c) XPS survey spectrum, and core-level spectra of (d) P 2p, (f) Ni 2p and (g) Mn 2p for LNCM and P-LNCM samples; (e) FTIR spectra, (h, i) XRD diffractograms of LNCM and P-LNCM samples; the inset in e is the magnified FTIR curves, the insets in h and i are magnified XRD patterns.

agreement with Ni^{2+} and Ni^{3+}, respectively. In addition, the average valence of surface Ni cations in the P-LNCM sample is lower than that of LNCM sample. For the Mn cations, as shown in Fig. 1g, most Mn ions exist in the form of Mn^{4+} ($2p_{3/2}$, 642.8 eV) and Mn^{3+} ($2p_{3/2}$, 641.9 eV) for the two samples, but the Mn^{2+} ($2p_{3/2}$, 641.1 eV) can be detected in the P-LNCM sample. These indicate a small reduction of Ni and Mn on the material surface after PH_3 treating. The core-level spectra of Co 2p are displayed in Fig. S2. The valence of Co ions shows no change before and after modification, maintaining the valence of III. All those pieces of evidence indicate that the oxidation states of surficial Ni and Mn ions were reduced after PH_3 treatment, and the $(PO_4)^{3-}$ groups with strong P–O bonds were successfully introduced into the surface of the modified material. As discussed in Introduction, the strong P–O bonds in $(PO_4)^{3-}$ groups are in favor of stabilizing local oxygen environment and further inhibiting surface O_2 release. Meanwhile, the rather strong P–O bonds in polyanion PO_4 and the covalent bonds between polyanion $(PO_4)^{3-}$ and $TM^{2+/3+}$ ensure the compounds ($LiTMPO_4$) electrochemically stable at high potential.

The structure of the surface protection layer formed on the P-LNCM after treatment was further characterized by XRD. As shown in Fig. 1h and i, all strong diffraction peaks are well indexed to the *R*-3*m* space group attributed to the hexagonal $LiTMO_2$ phase, and the weak superlattice diffraction feature (20–23°) could be attributed to the monoclinic Li_2MnO_3 phase with *C*2/*m* space group. Meanwhile, a small amount of spinel phase (*Fd*-3*m* space group) is found in both LNCM and P-LNCM, and the proportion of spinel phase in the P-LNCM sample is higher than that of LNCM sample, which can be inferred from the broadening of the (003) peak in the P-LNCM sample (middle panel of Fig. 1h) [50,51]. This can also be confirmed by the Raman spectra (the blue region near 610 cm^{-1} is assigned to the Mn–O stretching vibrations in spinel $Li_4Mn_5O_{12}$ structure, shown in Fig. S3) [52]. Interestingly, a small peak can be found at 22.45° (inset in Fig. 1h) in the XRD pattern of P-LNCM, indexed to the (120) diffraction peak of the $LiMnPO_4$ phase (PDF#33-0804) [53], which is consistent with the results of XPS and FTIR. Limited by the surface gas-solid reaction (short reaction time), just a small amount of P was introduced into the material, evidenced by the ICP-OES, SEM, XPS, and FTIR results. Therefore, the characteristic diffraction peak of $LiMnPO_4$ phase is weak. Besides, the Fig. 1h middle panel shows that the intensity of (003) peak reduces after PH_3-treating, while there is no obvious change on (104) peak (Fig. 1h right panel). According to previous reports [54], the intensity ratio of (003) to (104) peak ($I_{(003)}/I_{(104)}$) can be used to evaluate the cation order degree in layered oxide cathode materials. After surface modification, the $I_{(003)}/I_{(104)}$ value decreases, implying a higher degree of cation disorder in P-

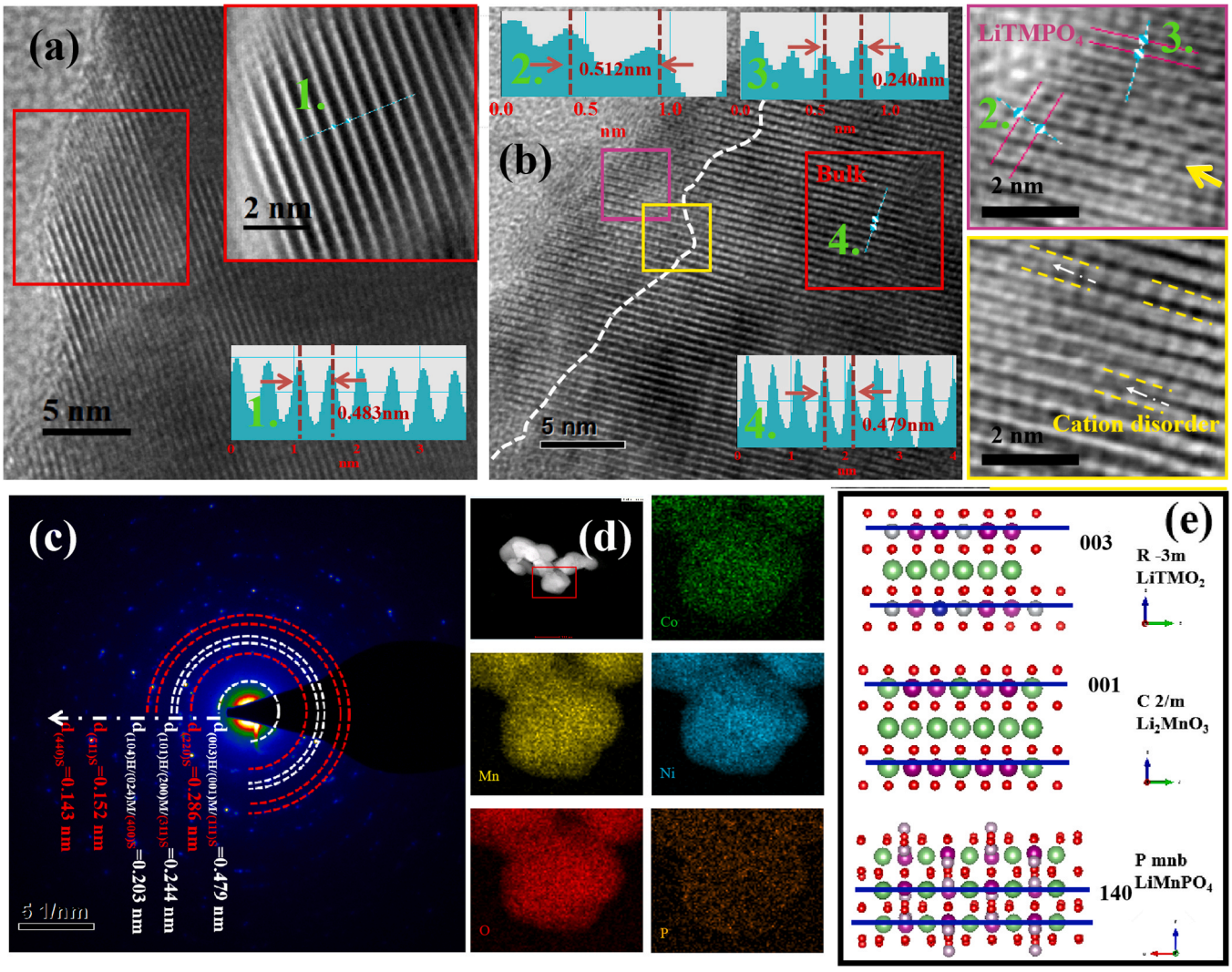

Fig. 2. HRTEM images of LNCM (a) and P-LNCM (b) samples and the corresponding line profiles of the Z-contrast information with the measured spacing of TM layer; (c) the index of electron diffraction rings of P-LNCM sample reveals layered structures and spinel cubic structures; (d) STEM image and the corresponding EDS mapping of P-LNCM sample; (e) simulative crystal structure of $LiTMO_2$ phase (*R*-3*m* space group), Li_2MnO_3 phase (*C*2/*m* space group) and $LiMnPO_4$ phase (*Pmnb* space group).

LNCM relative to LNCM. The degree of doublet splitting of (006)/(102) and (108)/(110) peak pairs is also a clear indicator of the hexagonal ordering (indexed the layer structure) [55]. Compared with the pristine LNCM sample, the splitting of (006)/(102) and (108)/(110) peak pairs of the P-LNCM sample becomes inconspicuous (Fig. 1i), which also means increased disordering of cations after surface treatment.

To further probe the evolution of surface structure after modification, the high-resolution transmission electron microscope (HRTEM) measurement was carried out to characterize the morphologies of the as-prepared samples at the nanoscale, and the results are shown in Fig. 2. It can be found that the bulk of P-LNCM sample still retains a well-layered structure same as the LNCM sample (Fig. 2a and b, red square regions), corresponding to the layered structure with *R*-3*m* space group, e.g. α-$NaFeO_2$. The interplanar spacing (ca. 0.48 nm) of the lattice planes is indexed to the (003) fringes of LNCM (Fig. 2e). The selected area electron diffraction (SAED) pattern of P-LNCM (Fig. 2c) indicates the existence of layered Li_2MnO_3 phase, $LiTMO_2$ phase, and spinel $Li_4Mn_5O_{12}$ phase, which is consistent with the XRD and Raman results. However, there is a remarkable difference in the surface region between P-LNCM and pristine LNCM. P-LNCM features an obvious interface layer with a thickness of 5–10 nm at the surface, which consists of cation disordered structure and $LiMnPO_4$-like phase. As shown in the magnified yellow region in Fig. 2b, an interlayer of cations appears in between the (003) lattice planes, indicative of the formation of the cation disordered phase close to the bulk region. This is also in good agreement with the increased cation disorder as evidenced by XRD results. Besides, at the outer zone of the surface layer, the HRTEM image shows the features of $LiMnPO_4$-like phase with lattice spacings of 0.240 and 0.512 nm (the region of the pink square), which correspond to the (140) and (020) lattice planes of $LiMnPO_4$ with *Pmnb* space group (PDF#33-0804, Fig. 2e), respectively. The evolution of surface structure was speculated to be an *in-situ* self-reconstruction process. Both the cation disordered phase and $LiMnPO_4$-like phase originate from the migration of surface TM ions into the Li layer during the thermal treatment. Besides, in the PH_3 treatment process, $(PO_4)^{3-}$ groups were introduced and combined with the rearranged cations to form $LiMnPO_4$-like phase. Eventually, a mixed-phase surface layer was formed as shown in Scheme 1. The STEM image and the corresponding EDS maps of P-LNCM (Fig. 2d) further reveal the morphology and elemental distribution of the P-LNCM sample. It shows that P was successfully introduced into the primary particles and keeps a uniform distribution with Ni, Co, Mn, and O elements. Based on the above discussion, the surface mixed modification layer was produced by an *in-situ* surface self-reconstruction process, which ensures the structural continuity of the surface modification layer with the bulk.

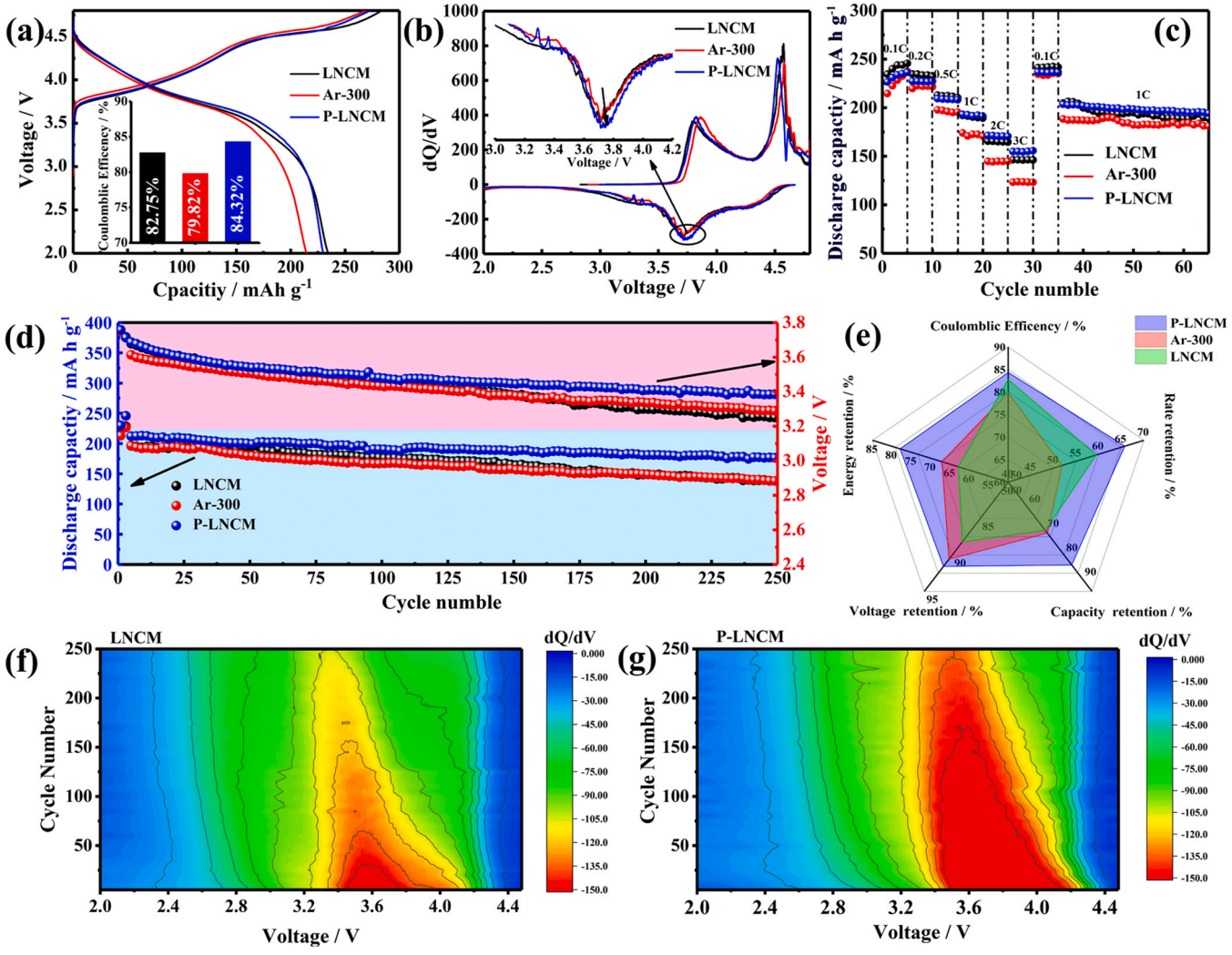

Fig. 3. Electrochemical performance of LNCM, Ar-300 and P-LNCM samples at 25 °C and 2.0–4.8 V. (a) The initial charge/discharge curves and Coulombic Efficiency (illustration) at 0.1 C; (b) the corresponding initial dQ/dV curves; (c) Rate performance; (d) cycle performance (below) and average discharge voltage (above) of samples at 1 C; (e) Performance comparison. Differential discharge capacity curves of (f) LNCM and (g) P-LNCM electrode obtained from the discharge curves every five cycles during the cycling tests.

Both phases in this modification layer are capable of stabilizing the surface lattice oxygen and mitigating the side reaction with electrolyte.

To evaluate the effect of surface modification on the electrochemical performance, the electrochemical tests were conducted on the as-prepared electrodes at different current densities (1 C = 250 mA g^{-1}) with the voltage range of 2.0–4.8 V. Fig. 3a and b show the initial charge/discharge curves and the corresponding dQ/dV curves of LNCM, Ar-300 and P-LNCM electrodes. All samples exhibit typical stair-like charge and S-shaped discharge characteristic curves for high-Ni content Li-rich cathode materials [30]. In Fig. 3a, the modified electrodes of Ar-300 electrode and P-LNCM electrode deliver a lower charge capacity at 0.1 C than the pristine LNCM electrode due to the release of Li_2O during heat treatment. Moreover, as shown in the inset of Fig. 3a, the initial Coulombic Efficiency (CE) of P-LNCM electrode (84.32%) is higher than that of LNCM electrode (82.75%), implying better redox reversibility. In Fig. 3b, an intense peak at a potential of about 4.5 V in the charge curves of dQ/dV plots corresponds to the activation of Li_2MnO_3 phase accompanied by a serious O_2 release. Compared with the LNCM sample, a lower peak intensity at a potential > 4.5 V in the P-LNCM sample can be observed during the charging process, implying a decreased O_2 loss and a more stable surface lattice oxygen [30]. On the contrary, during the discharging process, the reduction peak intensity (located at about 3.75 V) of the P-LNCM sample is higher than that of pristine LNCM sample, and this reduction peak shifts to slightly higher potential after surface modification. However, the peak of the P-LNCM located below 3.5 V is lower than that of the pristine LNCM sample. This indicated that the capacity of P-LNCM sample is preferred to release at high potential, resulting in higher operating voltage. Fig. 3c shows the rate performance of these samples. Compared with the pristine LNCM and Ar-300, P-LNCM displays better rate capability at higher current density.

Furthermore, the long-term cycling performances of the as-prepared samples are examined at 1 C in the voltage range of 2.0–4.8 V as shown in Fig. 3d and S4. Before the cycling test, the as-built cells were activated at 0.1 C for 3 cycles. It shows that the P-LNCM delivered a higher specific capacity of 176.7 mA h g^{-1} after 250 cycles at 1 C, which is much higher than 138.1 mA h g^{-1} of LNCM and 138.0 mA h g^{-1} of Ar-300. This corresponds to a capacity retention of 84.1% for P-LNCM, 69.9% for LNCM, and 71.0% for Ar-300 after 250 cycles. Meanwhile, compared with LNCM (1.7 mV voltage decay per cycle), the modified sample P-

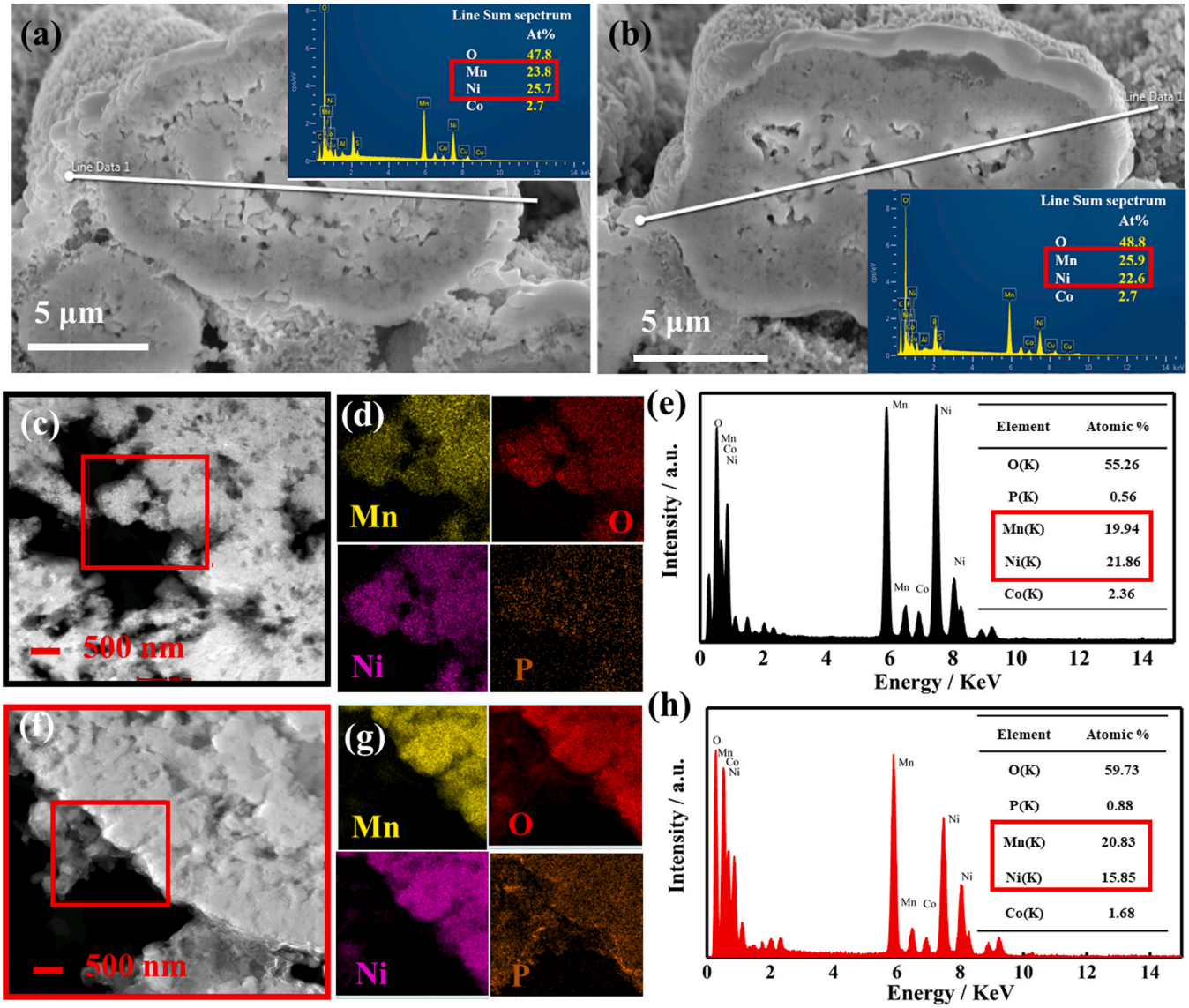

Fig. 4. The cross-section SEM images and the corresponding EDS line scan sum spectrum of LNCM (a) and P-LNCM samples (b) after cycling at 1 C; STEM images, the corresponding elemental mapping in red square and the corresponding EDS spectrum of LNCM (c–e) and P-LNCM (f–h) electrodes after cycling, respectively. The cycled electrode was cut by FIB, the thickness of (c and f) electrodes is about 200 nm.

LNCM displays a lower voltage fade rate of 1.2 mV per cycle, resulting in a higher operating voltage after cycling. The superior electrochemical performance of P-LNCM in terms of high operating voltage, high capacity and voltage retention can be directly confirmed by dQ/dV curves which were obtained from every five cycles of the discharge curves during the cycling tests (Fig. 3f and g). The intensity and position of the dQ/dV peak are relevant to the discharge capacity and the redox reaction potential, respectively. As shown in Fig. 3f, with the increase of cycle number, the peak intensity of LNCM shows a continuous decrease, which is more serious after 150 cycles. Besides, there is a huge shift in the peak position of LNCM from 3.6 V to ~ 3.3 V after 250 cycles. These imply a serious capacity decay and operating voltage attenuation in LNCM. In contrast, as shown in Fig. 3g, the peak position of P-LNCM starts from about 3.7 V; the peak intensity and the peak position can be maintained well after 250 cycles, indicating the cycling stability in terms of capacity and voltage. Based on the enhanced capacity retention and lower voltage decay rate, P-LNCM exhibited a twofold improvement of energy density retention (77.9% after 250 cycles at 1 C) compared to pristine LNCM (62.8%). Overall, after the surface treatment, the enhanced electrochemical performance was achieved, which is summarized in Fig. 3e. The enhanced electrochemical performance of P-LNCM electrode should be closely related to the multifunction surface protective layer. $LiTMPO_4$-like phase featuring the ability against high potential is responsible for preventing side reactions between electrode and electrolyte, and further reduces the dissolution of Mn during cycling (to be discussed in Fig. 4). Both the $LiTMPO_4$-like phase and the surface cation disorder phase contribute to stabilizing surface lattice oxygen structure and limiting surface O_2 release.

To further understand the working mechanism of the surface protective layer in P-LNCM, the changes of the morphology, the elemental composition and elemental distribution, and the microstructure of both cycled LNCM and P-LNCM electrodes were studied by FIB-SEM-EDS, HRTEM and EDS mapping; the results are exhibited in Fig. 4. The cross-sectional FIB-SEM images and line scans element analysis of LNCM and P-LNCM electrodes before and after cycling are shown in Fig. S1, 4a and b. Regardless of the pristine LNCM sample or the P-LNCM sample, there is no significant change in morphology before and after cycling. However, the elemental composition of LNCM electrode displays an obvious change after cycling. As shown in Fig. 4a and b, the elemental ratio of Mn to Ni in cycled LNCM is much lower than that of cycled P-LNCM and the initial LNCM, meaning severe Mn dissolution in LNCM after long-term cycles. In other words, the decreased Mn dissolution in P-LNCM is attributed to the mixed-phase protective layer formed on the surface of the particles which can stabilize surface lattice oxygen and suppress the side reactions between electrode and electrolyte. To further accurately investigate the spatial distribution and composition of the Mn element, the cycled electrode particles were cut to 200 nm by FIB (Fig. S5), and the elemental distribution and composition were probed by STEM-EDS. As shown in Fig. 4d and g, the elements of Ni, O, and P of the cycled LNCM electrode are distributed uniformly in the sample and the distribution of Mn seems to be uneven. This implies the dissolution of Mn in LNCM after long-term cycles. As for the P-LNCM electrode, enriched element P on the surface layer can be observed along with uniformly distributed Ni, Co, Mn and O, which also suggests the existence of the $LiMnPO_4$-like protective layer in this sample. Meanwhile, the elemental composition analysis of STEM-EDS further confirms the

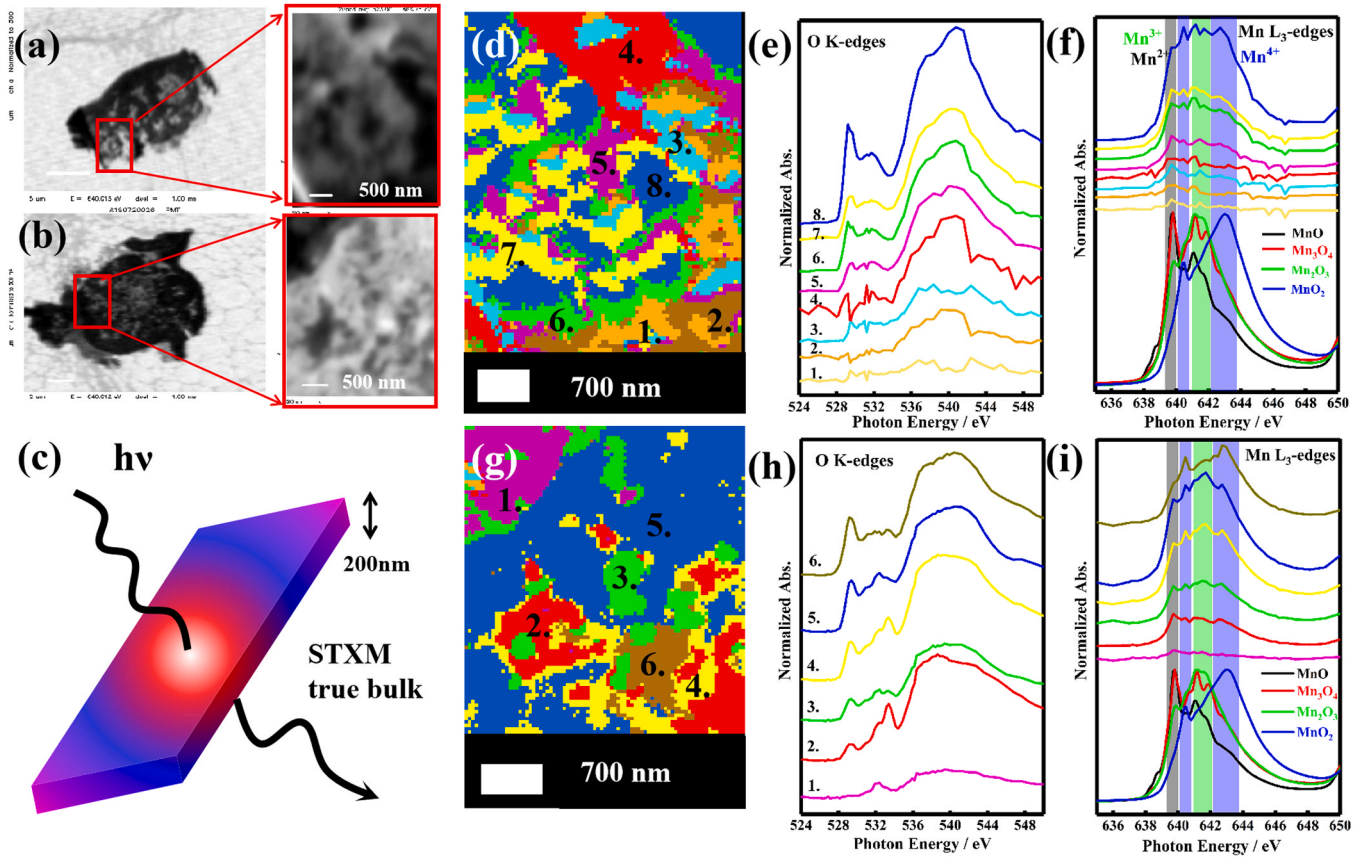

Fig. 5. Morphology mapping of cycled Pristine LNCM (a) and P-LNCM (b) electrode by STXM; (c) schematic illustration of the principle of bulk sensitive STXM; quasi-quantitative chemical phase map of Pristine (d, the phases with different chemical composition and oxidation state are marked as *1.* to *8.*) and P-LNCM (g, the phases with different chemical composition and oxidation state are marked as *1.* to *6.*); the normalized O K-edge (e and h), and Mn L_3-edge (f and i) XAS spectra of the regions marked in Pristine (e and f) and P-LNCM (h and i) electrodes after cycling. The standard XAS of Mn L_3-edge obtained in MnO, Mn_2O_3, Mn_3O_4 and MnO_2 are included at the bottom of (f) and (i).

dissolution of Mn ions of LNCM sample after long-term cycling, in agreement with FIB-SEM-EDS results.

The analysis of morphology and chemical states at high spatial resolution is crucial for elucidating the degradation mechanism of Li-ion cathode materials. To further explore the protective effect of the modified surface layer, the cycled LNCM and P-LNCM electrodes were also investigated by bulk sensitive STXM at the Spectromicroscopy (SM) beamline of the Canadian Light Source (CLS), as shown in Fig. 5. The bulk sensitive STXM combines microscopy technology with synchrotron based XAS method, enabling nanoscale chemical imaging with a spatial resolution of around 30 nm as well as fine energy resolution. The cross-sectional samples for TEM and STXM characterization were prepared by FIB and the sample preparation processes are shown in Fig. S5a. As seen from the TEM and SAED patterns, the cycled P-LNCM electrode remains a well-layered structure compared with the poor crystallinity of cycled LNCM electrode, and detailed information is described in the Supporting information Fig. S5. STXM was successfully applied to reveal phase separation in the lithiation process of olivine structure electrodes [56,57]. In this work, STXM was used to probe the high spatial resolution chemical distribution and oxidation state of TM cations in LR-NCM with complex phases and multi-elemental composition. Fig. 5a and b display the morphology mapping of the selected sample regions of the cycled electrodes with a thickness of 200 nm (this can ensure accurate true bulk sensitivity of STXM without signal saturation, Fig. 5c). The chemical phase distribution of the cycled LNCM and P-LNCM electrodes obtained by the principal component analysis (PCA) are displayed in Fig. 5d and g, respectively. Different colors represent different chemical phase with the different oxidation state of TM cations and different local electronic structure environment. The phases with different chemical composition and oxidation state are marked as *1.* to *8.* for the cycled LNCM electrode and *1.* to *6.* for the cycled P-LNCM electrode. It can be seen that the integrity of the chemical phases of the cycled LNCM electrode is poor, while the cycled P-LNCM electrode maintains good integrity of the chemical phases. Such phase separation difference indicates a severe structure degradation in the primary particle level in LNCM as compared to a less degradation in P-LNCM, which could be attributed to the beneficial effect of surface protection layer in P-LNCM. The chemical mapping thus unambiguously confirms that the *in-situ* surface self-reconstruction process during PH_3 treatment ensures the structural integrality and continuity of the surface modification layer to the bulk, and importantly forms a mixed-phase protective layer. This protective layer can effectively suppress the occurrence of the interface side reactions during long cycling, thereby preventing the electrode from being corroded by the electrolyte.

The soft X-ray XAS spectra, extracted from STXM data, at O K-edge, Mn L_3-edge, Co L_3-edge and Ni L_3-edge in the marked regions (Fig. 5d and g) of cycled LNCM and P-LNCM electrodes are displayed in Fig. 5e, f, h, i and Fig. S6. Standard compounds, including MnO, Mn_3O_4, Mn_2O_3, and MnO_2, were also measured and their Mn L_3 XAS spectra are included in Fig. 5f and i; the Mn oxidation state in different chemical phases can be determined based on the relative intensity of the peaks in Mn XAS. From the chemical phase map in Fig. 5d and the Mn L_3-edges XAS spectra of cycled LNCM electrode in Fig. 5f, it can be concluded that: a) many particles have Mn^{2+} and Mn^{3+} component; b) many particles have more than one chemical component; c) Mn^{4+} spectrum can hardly be detected (by reference to the standard MnO_2, it can also be seen in Fig. S7a and b). This means that the valence state of Mn of LNCM electrode without any surface treatment suffers from severe reduction after long-term cycling, which directly leads to the voltage fade and capacity decay. Different from the cycled LNCM electrode, the surface-modified electrode maintains good chemical phase integrity and a higher oxidation state of TM cations after long-term cycling. As can be seen in Fig. 5g and i, most particles of cycled P-LNCM electrode are dominated by Mn^{3+} and Mn^{4+} spectrum can still be probed in the brown region (region 6. in Fig. 5g and the blue region in Fig. S7c). The statistical quality in the Mn spectrum of P-LNCM is much better along with a higher edge jump relative to that in LNCM, which again confirms less Mn dissolution in P-LNCM as being observed in SEM and TEM studies. These results highlight the protective roles of the PH_3-modified layer on the surface of the electrode particles to ensure the voltage and capacity stability of the material when cycling at a high potential. Interestingly, the O K-edges XAS spectra of cycled P-LNCM shows enhanced spectroscopic feature at above 532 eV relative to that below 530 eV, especially at phase regions *2.* and *4.4.*; this is different from that in LNCM with normal t_{2g}-e_g splitting as being expected in TM–O covalent bonding environment [58]. This distorted TM–O bond can be inferred as either a direct influence of strong P–O bonds and/or the cation disorder phase in P-LNCM, or a subsequent effect being generated during cycling. Regardless of what the exact working mechanism is, this protection layer efficiently stabilizes the lattice oxygen structure and resists the continuous reduction of TM ions during cycling.

4. Conclusions

In summary, an *in-situ* self-reconstruction strategy has been proposed and developed to simultaneously optimize the surface chemical composition and the local structure in high energy density Li-rich cathodes. Specifically, the multifunction protective layer, consisting of the cation disorder phase and the $LiTMPO_4$-like phase, was produced by a simple PH_3 gas treatment at low temperature. The formed multifunction mixed-phase protective layer has the following advantages: 1) Ensuring the structural integrity and continuity of the protective layer to the bulk structure; 2) Stabilizing the surface lattice oxygen and inhibiting the oxygen release by the cation disorder structure phase and strong P–O bonds; 3) Enabling the stability under high voltage cycling due to the formation of surface $LiTMPO_4$-like phase; 4) Suppressing interface side reactions between the electrode and the electrolyte, further effectively inhibiting the dissolution of TM ions. These positive effects result in a large enhancement in the stability of capacity and voltage during long charge/discharge cycles of the PH_3-modified sample. Besides, the bulk sensitive STXM with high spatial resolution and chemical sensitivity directly show that the modified sample maintains better chemical phase integrity and higher oxidation state of TM cations after long-term cycling compared to the pristine sample. All of these highlights the protective roles of the multifunction layer on the bulk of the electrode particles in maintaining the voltage and capacity stability of the material cycling at a high potential. This simple yet effective modification strategy provides a new path for guiding the interface design of high energy density cathode.

CRediT authorship contribution statement

Gang Sun: Conceptualization, Formal analysis, Investigation, Writing - original draft. **Changtai Zhao:** Formal analysis, Investigation, Writing - review & editing. **Fu-Da Yu:** Formal analysis, Investigation, Writing - review & editing. **Ruizhi Yu:** Investigation, Writing - review & editing. **Jian Wang:** Investigation, Writing - review & editing. **Jigang Zhou:** Investigation, Writing - review & editing. **Guangjie Shao:** Supervision, Investigation, Resources, Writing - review & editing. **Xueliang Sun:** Supervision, Investigation, Resources, Writing - review & editing. **Zhen-Bo Wang:** Supervision, Investigation, Resources, Writing - review & editing.

Declaration of Competing Interest

The authors declare that they have no known competing financial interests or personal relationships that could have appeared to influence the work reported in this paper.

Acknowledgement

The authors acknowledge the financial support from the National

Natural Science Foundation of China (Grant Nos. 51674221, 51704261 and 51902072) and China Postdoctoral Science Foundation (Grant Nos. 2017M621285 and 2018T110292) and the Natural Science Foundation of Hebei Province (B2018203330 and B2018203360). CLS is supported by the Canada Foundation for Innovation (CFI), the Natural Sciences and Engineering Research Council of Canada (NSERC), the National Research Council (NRC), the Canadian Institutes of Health Research (CIHR), the Government of Saskatchewan, and the University of Saskatchewan. G.S. acknowledges financial support from the China Scholarship Council (CSC).

Appendix A. Supporting information

Supplementary data associated with this article can be found in the online version at doi:10.1016/j.nanoen.2020.105459.

References

[1] M. Armand, J.M. Tarascon, Building better batteries, Nature 7179 (451) (2008) 652–657.
[2] B. Obama, The irreversible momentum of clean energy, Science 6321 (355) (2017) aam6284.
[3] Y. Ding, Z.P. Cano, A. Yu, J. Lu, Z. Chen, Automotive Li-ion batteries: current status and future perspectives, Electrochem. Energy Rev. 1 (2) (2019) 1–28.
[4] W. Li, B. Song, A. Manthiram, High-voltage positive electrode materials for lithium-ion batteries, Chem. Soc. Rev. 10 (46) (2017) 3006–3059.
[5] B. Ammundsen, J. Paulsen, Novel lithium-ion cathode materials based on layered manganese oxides, Adv. Mater. 12–13 (13) (2001) 943–+.
[6] H. Maleki Kheimeh Sari, X. Li, Controllable cathode–electrolyte interface of Li [Ni0.8Co0.1Mn0.1]O2 for lithium ion batteries: a review, Adv. Energy Mater. 39 (9) (2019) 1901597.
[7] Q. Xu, X. Li, H.M. Kheimeh Sari, W. Li, W. Liu, Y. Hao, J. Qin, B. Cao, W. Xiao, Y. Xu, Y. Wei, L. Kou, Z. Tian, L. Shao, C. Zhang, X. Sun, Surface engineering of LiNi0.8Mn0.1Co0.1O2 towards boosting lithium storage: bimetallic oxides versus monometallic oxides, Nano Energy 77 (2020), 105034.
[8] W. Liu, X. Li, D. Xiong, Y. Hao, J. Li, H. Kou, B. Yan, D. Li, S. Lu, A. Koo, K. Adair, X. Sun, Significantly improving cycling performance of cathodes in lithium ion batteries: the effect of Al2O3 and LiAlO2 coatings on LiNi0.6Co0.2Mn0.2O2, Nano Energy 44 (2018) 111–120.
[9] S. Hu, A.S. Pillai, G. Liang, W.K. Pang, H. Wang, Q. Li, Z. Guo, Li-rich layered oxides and their practical challenges: recent progress and perspectives, Electrochem. Energy Rev. 2 (2) (2019) 277–311.
[10] D. Eum, B. Kim, S.J. Kim, H. Park, J. Wu, S. Cho, G. Yoon, M.H. Lee, S. Jung, W. Yang, W.M. Seong, K. Ku, O. Tamwattana, S.K. Park, I. Hwang, K. Kang, Voltage decay and redox asymmetry mitigation by reversible cation migration in lithium-rich layered oxide electrodes, Nat. Mater. (2020).
[11] R. Yu, Z. Zhang, S. Jamil, J. Chen, X. Zhang, X. Wang, Z. Yang, H. Shu, X. Yang, Effects of nanofiber architecture and antimony doping on the performance of lithium-rich layered oxides: enhancing lithium diffusivity and lattice oxygen stability, ACS Appl. Mater. Interfaces 19 (10) (2018) 16561–16571.
[12] B. Li, D. Xia, Anionic redox in rechargeable lithium batteries, Adv. Mater. 48 (29) (2017) 1701054.
[13] G. Assat, J. Tarascon, Fundamental understanding and practical challenges of anionic redox activity in Li-ion batteries, Nat. Energy 5 (3) (2018) 373–386.
[14] S. Myeong, W. Cho, W. Jin, J. Hwang, M. Yoon, Y. Yoo, G. Nam, H. Jang, J. Han, N. Choi, M.G. Kim, J. Cho, Understanding voltage decay in lithium-excess layered cathode materials through oxygen-centred structural arrangement, Nat. Commun. 1 (9) (2018).
[15] E. Hu, X. Yu, R. Lin, X. Bi, J. Lu, S. Bak, K. Nam, H.L. Xin, C. Jaye, D.A. Fischer, K. Amine, X. Yang, Evolution of redox couples in Li- and Mn-rich cathode materials and mitigation of voltage fade by reducing oxygen release, Nat. Energy 8 (3) (2018) 690–698.
[16] G. Assat, D. Foix, C. Delacourt, A. Iadecola, R. Dedryvère, J. Tarascon, Fundamental interplay between anionic/cationic redox governing the kinetics and thermodynamics of lithium-rich cathodes, Nat. Commun. 1 (8) (2017).
[17] P. Yan, J. Zheng, T. Chen, L. Luo, Y. Jiang, K. Wang, M. Sui, J. Zhang, S. Zhang, C. Wang, Coupling of electrochemically triggered thermal and mechanical effects to aggravate failure in a layered cathode, Nat. Commun. 1 (9) (2018).
[18] F. Dogan, B.R. Long, J.R. Croy, K.G. Gallagher, H. Iddir, J.T. Russell, M. Balasubramanian, B. Key, Re-entrant lithium local environments and defect driven electrochemistry of Li- and Mn-rich Li-ion battery cathodes, J. Am. Chem. Soc. 6 (137) (2015) 2328–2335.
[19] G. Assat, A. Iadecola, D. Foix, R. Dedryvère, J. Tarascon, Direct quantification of anionic redox over long cycling of Li-rich NMC via hard X-ray photoemission spectroscopy, ACS Energy Lett. 11 (3) (2018) 2721–2728.
[20] W.E. Gent, K. Lim, Y. Liang, Q. Li, T. Barnes, S. Ahn, K.H. Stone, M. McIntire, J. Hong, J.H. Song, Y. Li, A. Mehta, S. Ermon, T. Tyliszczak, D. Kilcoyne, D. Vine, J. Park, S. Doo, M.F. Toney, W. Yang, D. Prendergast, W.C. Chueh, Coupling between oxygen redox and cation migration explains unusual electrochemistry in lithium-rich layered oxides, Nat. Commun. 2091 (8) (2017).
[21] M. Hekmatfar, A. Kazzazi, G.G. Eshetu, I. Hasa, S. Passerini, Understanding the electrode/electrolyte interface layer on the Li-rich nickel manganese cobalt layered oxide cathode by XPS, ACS Appl. Mater. Interfaces 46 (11) (2019) 43166–43179.
[22] Z. Lun, B. Ouyang, D.A. Kitchaev, R.J. Clément, J.K. Papp, M. Balasubramanian, Y. Tian, T. Lei, T. Shi, B.D. McCloskey, J. Lee, G. Ceder, Improved cycling performance of Li-excess cation-disordered cathode materials upon fluorine substitution, Adv. Energy Mater. 2 (9) (2019) 1802959.
[23] D. Liu, X. Fan, Z. Li, T. Liu, M. Sun, C. Qian, M. Ling, Y. Liu, C. Liang, A cation/anion co-doped Li1.12Na0.08Ni0.2Mn0.6O1.95F0.05 cathode for lithium ion batteries, Nano Energy (58) (2019) 786–796.
[24] Q. Li, D. Zhou, L. Zhang, D. Ning, Z. Chen, Z. Xu, R. Gao, X. Liu, D. Xie, G. Schumacher, X. Liu, Tuning anionic redox activity and reversibility for a high-capacity Li-rich Mn-based oxide cathode via an integrated strategy, Adv. Funct. Mater. (2019) 1806706.
[25] R. Yu, X. Zhang, T. Liu, L. Yang, L. Liu, Y. Wang, X. Wang, H. Shu, X. Yang, Spinel/layered heterostructured lithium-rich oxide nanowires as cathode material for high-energy lithium-ion batteries, ACS Appl. Mater. Interfaces 47 (9) (2017) 41210–41223.
[26] H. Yu, Y. So, Y. Ren, T. Wu, G. Guo, R. Xiao, J. Lu, H. Li, Y. Yang, H. Zhou, R. Wang, K. Amine, Y. Ikuhara, Temperature-sensitive structure evolution of lithium–manganese-rich layered oxides for lithium-ion batteries, J. Am. Chem. Soc. 45 (140) (2018) 15279–15289.
[27] J. Shi, D. Xiao, M. Ge, X. Yu, Y. Chu, X. Huang, X. Zhang, Y. Yin, X. Yang, Y. Guo, L. Gu, L. Wan, High-capacity cathode material with high voltage for Li-ion batteries, Adv. Mater. 9 (30) (2018) 1705575.
[28] K. Ku, J. Hong, H. Kim, H. Park, W.M. Seong, S. Jung, G. Yoon, K. Park, H. Kim, K. Kang, Suppression of voltage decay through manganese deactivation and nickel redox buffering in high-energy layered lithium-rich electrodes, Adv. Energy Mater. 21 (8) (2018) 1800606.
[29] P. Liu, H. Zhang, W. He, T. Xiong, Y. Cheng, Q. Xie, Y. Ma, H. Zheng, L. Wang, Z. Zhu, Y. Peng, L. Mai, D. Peng, Lithium deficiencies engineering in Li-rich layered oxide Li1.098Mn0.533Ni0.113Co0.138O2 for high-stability cathode, J. Am. Chem. Soc. 27 (141) (2019) 10876–10882.
[30] G. Sun, F. Yu, L. Que, L. Deng, M. Wang, Y. Jiang, G. Shao, Z. Wang, Local electronic structure modulation enhances operating voltage in Li-rich cathodes, Nano Energy 66 (2019), 104102.
[31] S. Kalluri, M. Yoon, M. Jo, H.K. Liu, S.X. Dou, J. Cho, Z. Guo, Feasibility of cathode surface coating technology for high-energy lithium-ion and beyond-lithium-ion batteries, Adv. Mater. 48 (29) (2017) 1605807.
[32] Y. Liu, Z. Yang, J. Li, B. Niu, K. Yang, F. Kang, A novel surface-heterostructured Li1.2Mn0.54Ni0.13Co0.13O2@ Ce0.8Sn0.2O2s cathode material for Li-ion batteries with improved initial irreversible capacity loss, J. Mater. Chem. A 28 (6) (2018) 13883–13893.
[33] F. Yu, L. Que, C. Xu, M. Wang, G. Sun, J. Duh, Z. Wang, Dual conductive surface engineering of Li-rich oxides cathode for superior high-energy-density Li-Ion batteries, Nano Energy 59 (2019) 527–536.
[34] X. Zhang, X. Xie, R. Yu, J. Zhou, Y. Huang, S. Cao, Y. Wang, K. Tang, C. Wu, X. Wang, Improvement of the cycling stability of Li-rich layered Mn-based oxide cathodes modified by nanoscale LaPO4 coating, ACS Appl. Energy Mater. 5 (2) (2019) 3532–3541.
[35] M. Wang, F. Yu, G. Sun, D. Gu, Z. Wang, Optimizing the structural evolution of Li-rich oxide cathode materials via microwave-assisted pre-activation, ACS Appl. Energy Mater. 1 (8) (2018) 4158–4168.
[36] X. Zhang, J. Shi, J. Liang, Y. Yin, J. Zhang, X. Yu, Y. Guo, Suppressing surface lattice oxygen release of Li-rich cathode materials via heterostructured spinel $Li_4Mn_5O_{12}$ coating, Adv. Mater. 29 (30) (2018) 1801751.
[37] H. Guo, Z. Wei, K. Jia, B. Qiu, C. Yin, F. Meng, Q. Zhang, L. Gu, S. Han, Y. Liu, H. Zhao, W. Jiang, H. Cui, Y. Xia, Z. Liu, Abundant nanoscale defects to eliminate voltage decay in Li-rich cathode materials, Energy Storage Mater. (16) (2019) 220–227.
[38] B. Wu, X. Yang, X. Jiang, Y. Zhang, H. Shu, P. Gao, L. Liu, X. Wang, Synchronous tailoring surface structure and chemical composition of Li-rich-layered oxide for high-energy lithium-ion batteries, Adv. Funct. Mater. (2018) 1803392.
[39] B. Qiu, M. Zhang, L. Wu, J. Wang, Y. Xia, D. Qian, H. Liu, S. Hy, Y. Chen, K. An, Y. Zhu, Z. Liu, Y.S. Meng, Gas–solid interfacial modification of oxygen activity in layered oxide cathodes for lithium-ion batteries, Nat. Commun. (7) (2016) 12108.
[40] E.M. Erickson, H. Sclar, F. Schipper, J. Liu, R. Tian, C. Ghanty, L. Burstein, N. Leifer, J. Grinblat, M. Talianker, J. Shin, J.K. Lampert, B. Markovsky, A. I. Frenkel, D. Aurbach, High-temperature treatment of Li-rich cathode materials with ammonia: improved capacity and mean voltage stability during cycling, Adv. Energy Mater. 18 (7) (2017) 1700708.
[41] Z. Sun, L. Xu, C. Dong, H. Zhang, M. Zhang, Y. Ma, Y. Liu, Z. Li, Y. Zhou, Y. Han, Y. Chen, A facile gaseous sulfur treatment strategy for Li-rich and Ni-rich cathode materials with high cycling and rate performance, Nano Energy 63 (2019), 103887.
[42] Z. Chen, G. Kim, D. Bresser, T. Diemant, J. Asenbauer, S. Jeong, M. Copley, R. J. Behm, J. Lin, Z. Shen, S. Passerini, MnPO4-coated Li(Ni0.4Co0.2Mn0.4)O2 for lithium(-ion) batteries with outstanding cycling stability and enhanced lithiation kinetics, Adv. Energy Mater. 27 (8) (2018) 1801573.
[43] S. Yang, P. Wang, H. Wei, L. Tang, X. Zhang, Z. He, Y. Li, H. Tong, J. Zheng, Li4V2Mn(PO4)4-stablized Li[Li0.2Mn0.54Ni0.13Co0.13]O2 cathode materials for lithium ion batteries, Nano Energy (63) (2019), 103889.
[44] Z. Wu, S. Ji, T. Liu, Y. Duan, S. Xiao, Y. Lin, K. Xu, F. Pan, Aligned Li^+ tunnels in core–shell $Li(Ni_xMn_yCo_z)O_2$@$LiFePO_4$ enhances its high voltage cycling stability as Li-ion battery cathode, Nano Lett. 10 (16) (2016) 6357–6363.

[45] J. Wolfenstine, J. Allen, LiNiPO4–LiCoPO4 solid solutions as cathodes, J. Power Sources 1 (136) (2004) 150–153.
[46] H. Huang, C. Yu, C. Zhao, X. Han, J. Yang, Z. Liu, S. Li, M. Zhang, J. Qiu, Iron-tuned super nickel phosphide microstructures with high activity for electrochemical overall water splitting, Nano Energy (34) (2017) 472–480.
[47] S. Li, C. Yu, Y. Yang, X. Song, S. Chen, L. Song, B. Qiu, J. Yang, H. Huang, W. Guo, C. Zhao, M. Zhang, J. Qiu, Phosphate species up to 70% mass ratio for enhanced pseudocapacitive properties, Small 50 (14) (2018) 1803811.
[48] M. Wang, F. Yu, G. Sun, J. Wang, J. Zhou, D. Gu, Z. Wang, Co-regulating the surface and bulk structure of Li-rich layered oxides by a phosphor doping strategy for high-energy Li-ion batteries, J. Mater. Chem. A 14 (7) (2019) 8302–8314.
[49] X. Du, W. He, X. Zhang, Y. Yue, H. Liu, X. Zhang, D. Min, X. Ge, Y. Du, Enhancing the electrochemical performance of lithium ion batteries using mesoporous $Li_3V_2(PO_4)_3$/C microspheres, J. Mater. Chem. 13 (22) (2012) 5960.
[50] Y. Ma, P. Liu, Q. Xie, G. Zhang, H. Zheng, Y. Cai, Z. Li, L. Wang, Z. Zhu, L. Mai, D. Peng, Double-shell Li-rich layered oxide hollow microspheres with sandwich-like carbon@spinel@layered@spinel@carbon shells as high-rate lithium ion battery cathode, Nano Energy (59) (2019) 184–196.
[51] Y. Pei, Q. Chen, Y. Xiao, L. Liu, C. Xu, L. Zhen, G. Henkelman, G. Cao, Understanding the phase transitions in spinel-layered-rock salt system: criterion for the rational design of LLO/spinel nanocomposites, Nano Energy (40) (2017) 566–575.
[52] G. Sun, X. Yin, W. Yang, A. Song, C. Jia, W. Yang, Q. Du, Z. Ma, G. Shao, The effect of cation mixing controlled by thermal treatment duration on the electrochemical stability of lithium transition-metal oxides, Phys. Chem. Chem. Phys. 44 (19) (2017) 29886–29894.
[53] X. Zhao, L. An, J. Sun, G. Liang, $LiNi_{0.5}Co_{0.2}Mn_{0.3}O_2$-$LiMn_{0.6}Fe_{0.4}PO_4$ mixture with both excellent electrochemical performance and low cost as cathode material for power lithium ion batteries, J. Electrochem. Soc. 2 (165) (2018) A142–A148.
[54] D. Wang, R. Kou, Y. Ren, C. Sun, H. Zhao, M. Zhang, Y. Li, A. Huq, J.Y.P. Ko, F. Pan, Y. Sun, Y. Yang, K. Amine, J. Bai, Z. Chen, F. Wang, Synthetic control of kinetic reaction pathway and cationic ordering in high-Ni layered oxide cathodes, Adv. Mater. 39 (29) (2017) 1606715.
[55] Y. Chen, Y. Li, W. Li, G. Cao, S. Tang, Q. Su, S. Deng, J. Guo, High-voltage electrochemical performance of $LiNi_{0.5}Co_{0.2}Mn_{0.3}O_2$ cathode material via the synergetic modification of the Zr/Ti elements, Electrochim. Acta (281) (2018) 48–59.
[56] Y. Yu, M. Farmand, C. Kim, Y. Liu, C.P. Grey, F.C. Strobridge, T. Tyliszczak, R. Celestre, P. Denes, J. Joseph, H. Krishnan, F.R.N.C. Maia, A.L.D. Kilcoyne, S. Marchesini, T.P.C. Leite, T. Warwick, H. Padmore, J. Cabana, D.A. Shapiro, Three-dimensional localization of nanoscale battery reactions using soft X-ray tomography, Nat. Commun. 1 (9) (2018).
[57] M. Lu, F. Yu, Y. Hu, K. Zaghib, S.B. Schougaard, Z. Wang, J. Zhou, J. Wang, J. Goodenough, T.K. Sham, Correlative imaging of ionic transport and electronic structure in nano Li0.5FePO4 electrodes, Chem. Commun. (Camb.) 6 (56) (2020) 984–987.
[58] J. Zhou, D. Hong, J. Wang, Y. Hu, X. Xie, H. Fang, Electronic structure variation of the surface and bulk of a LiNi0.5Mn1.5O4 cathode as a function of state of charge: X-ray absorption spectroscopic study, Phys. Chem. Chem. Phys. 27 (16) (2014) 13838–13842.